Journal of Materials Chemistry C

ROYAL SOCIETY OF CHEMISTRY

PAPER

View Article Online
View Journal | View Issue

Cite this: J. Mater. Chem. C, 2024, 12, 6559

Excellent red upconversion luminescence in $GdLaO_3:Er^{3+}/Yb^{3+}/Sc^{3+}$ under 980 nm laser excitation†

Meiling Li,[a] Yongze Cao,*[a] Lihong Cheng,[a] Tianshuo Liu,[b] Yuhan Fan,[a] Jinsu Zhang[a] and Baojiu Chen*[a]

Received 14th March 2024,
Accepted 11th April 2024

DOI: 10.1039/d4tc01015a

rsc.li/materials-c

A series of $(Gd_{0.8-x}Er_{0.1}Yb_{0.1}Sc_x)LaO_3$ and $(Gd_{0.8}Er_{0.1}Yb_{0.1})(La_{1-x}Sc_x)O_3$ upconversion luminescence (UCL) phosphors were prepared by solid state sintering technology. The structure, diffuse reflection, and UCL spectra were investigated. $(Gd_{0.8}Er_{0.1}Yb_{0.1})(La_{0.9}Sc_{0.1})O_3$ represents excellent red UCL, which is comparable to commercial red β-$NaYF_4$:Er^{3+}/Yb^{3+}. Er^{3+}/Yb^{3+} are distributed in a continuous double layer structure, blocked by a single layer of Sc^{3+}/La^{3+}. This structure allows cross relaxation (CR) to occur only in the double-layer structure and improves the efficiency of energy transfer with CR in the double-layer, resulting in the emission of outstanding red UCL. Using the luminescence branching intensity ratio (LIR) technique, the maximum value of relative temperature sensitivity is calculated as 0.01295 K^{-1} at 303 K. $GdLaO_3:Er^{3+}/Yb^{3+}/Sc^{3+}$ has excellent pure red UCL and can be applied in luminescence display and temperature sensing.

1. Introduction

The upconversion luminescence (UCL) process is the process of absorbing multiple low-energy photons to emit a high-energy photon.[1] Due to this unique property, it can be widely used in solar cells,[2,3] sterilization,[4] anti-counterfeiting,[5,6] medical treatment,[7,8] temperature sensing,[9–11] and so on. The UCL phosphor is obtained by doping the luminescence center (Er^{3+}, Tm^{3+}, Ho^{3+}) and sensitization center (Yb^{3+}) into a suitable host. In general, this host structure determines the UCL intensity. Now, β-$NaYF_4$ is currently recognized as the optimal host.[12,13] However, the chemical stability of fluoride is poor, and there is certain toxicity, so there are certain limitations on the above applications. Therefore, the use of a non-toxic, chemically stable oxide as a host to replace fluoride is a reasonable choice. However, a large number of experimental studies have shown that the UCL intensity of oxide phosphors is usually much lower than that of fluoride. Therefore, obtaining oxide phosphors with UCL intensity comparable to β-$NaYF_4$ is a challenge.

There are four main factors affecting UCL intensity. (1) Low phonon energy can reduce the non-radiative transition and help to obtain high UCL intensity.[14,15] (2) The low symmetry of the luminous center helps to break the imprisonment of the 4f–4f transition and improve the UCL intensity.[16–18] (3) The appropriate distance of rare earth ions is helpful to transfer energy from the sensitized center to the luminescent center and enhance UCL intensity.[19] (4) Distribution of rare earth ions in the host:[20] a suitable distribution of rare earth ions in the host helps to reduce and enhance the cross relaxation (CR) between rare earth ions and can regulate the visible green and red emission ratio for Yb^{3+}/Er^{3+} co-doped samples.[21,22] In our previous study,[23–25] it was found that the $BiTa_7O_{19}$ host has low phonon energy and low luminescence center symmetry, while Er^{3+}/Yb^{3+} are distributed in a single layer, obtaining excellent pure green UCL. Based on the inspiration of the previous experiments, the search for a low phonon and low luminescent center symmetry oxide host with Er^{3+}/Yb^{3+} distributed in a continuous double layer structure and blocked by other atomic layers is expected to obtain excellent pure red-light emission. Based on the above analysis, a low phonon energy ($\sim$419 cm^{-1}) $GdLaO_3$ host with space group $C2/m$ (No. 12) is expected to be a good choice.[26,27] Gd^{3+}/La^{3+} and Gd^{3+} sites form a continuous double layer structure, which is blocked by a single layer of La^{3+}. Therefore, we regulate doping different elements so that Er^{3+}/Yb^{3+} replaces Gd^{3+}/La^{3+} and Gd^{3+} sites, making Er^{3+}/Yb^{3+} distribute in a double layer structure, blocked by a La^{3+} single layer, and it is expected to obtain outstanding red UCL intensity. Stronger absorption of biological tissues for green UCL than red UCL is observed. Therefore, red UCL can have a deeper tissue

[a] Department of Physics, Dalian Maritime University, Dalian, 116026, China. E-mail: cyz@dlmu.edu.cn, bjchen@dlmu.edu.cn
[b] Department of Physics and Astronomy, University College London, Gower St., London, WC1E 6BT, UK

† Electronic supplementary information (ESI) available. See DOI: https://doi.org/10.1039/d4tc01015a

detection depth, which is more suitable to be utilized in biomedical treatment.[28,29]

On the basis of Er^{3+}/Yb^{3+} co-doping, foreign ion doping to break the symmetry of the crystal field in the luminous center will significantly improve the UCL intensity. Some studies have shown that the smallest trivalent rare earth ion (Sc^{3+}) doping will decrease the crystal field symmetry and cause greater local structural distortion, leading to UCL enhancement.[30–32] Additionally, due to the small ionic radius and the same valence, Sc^{3+} ions can easily enter into other rare-earth-based host lattices as dopants for modulation of the crystallographic parameters toward UCL tuning.[33] Therefore, the sites occupied by $Er^{3+}/Yb^{3+}/Sc^{3+}$ can be controlled by changing the molar ratio of the raw materials to obtain excellent red UCL intensity in $Er^{3+}/Yb^{3+}/Sc^{3+}$ co-doped $GdLaO_3$ phosphors.

In this work, $(Gd_{0.8-x}Er_{0.1}Yb_{0.1}Sc_x)LaO_3$ (x = 0, 0.05, 0.1, 0.15, 0.2) and $(Gd_{0.8}Er_{0.1}Yb_{0.1})(La_{1-x}Sc_x)O_3$ (x = 0, 0.05, 0.1, 0.15, 0.2) phosphors were successfully prepared by high temperature solid phase sintering. $(Gd_{0.8}Er_{0.1}Yb_{0.1})(La_{0.9}Sc_{0.1})O_3$ has excellent red UCL intensity comparable to β-$NaYF_4$:Er^{3+}/Yb^{3+} under 980 nm laser excitation. Employing the luminescence branching intensity ratio (LIR) technique, the maximum value of relative temperate sensitivity of 0.01295 K^{-1} at 303 K was reached. $GdLaO_3$:$Er^{3+}/Yb^{3+}/Sc^{3+}$ is expected to replace β-$NaYF_4$:Er^{3+}/Yb^{3+} in the applied field of luminescence display and temperature sensing.

2. Experimental

2.1. Sample synthesis

All samples were prepared using the traditional high temperature solid state reaction method. The materials used in the production process included Gd_2O_3 (99.9%), La_2O_3 (99.9%), Er_2O_3 (99.9%), Yb_2O_3 (99.9%), and Sc_2O_3 (99.9%), weighed following the stoichiometric ratio. The weighed samples were mixed in an agate mortar, ground for 30 minutes, and then sintered in a resistance furnace at 1500 °C for 8 h. After the furnace cooling process was completed, the sintered samples were further ground into powders for the test.

2.2. Characterizations

Powder X-ray diffraction (XRD) analysis of the samples was conducted using a Rigaku X-ray diffractometer with Cu Kα radiation (λ = 1.5406 Å) in the 10°–90° range. The Rietveld refinement of the XRD data was performed with the general structural analysis system (GASA) software.[34] The diffuse reflectance spectra of the samples were analyzed using a UV3600 spectrophotometer (Shimadzu, Japan). The emission spectra of the samples at variable temperatures (303 to 663 K) were measured using a Hitachi F-4600 fluorescence spectrophotometer. Temperature control was achieved with a home-made device (DMU-TC 450), ensuring an accuracy better than ± 0.5 °C.

3. Results and discussion

Powder X-ray diffraction (XRD) pattern analysis was conducted to verify the crystal structure and phase purity of the synthesized phosphors. The XRD patterns are illustrated in Fig. 1(a) and (b). The diffraction peaks of the synthesized phosphors closely match the standard card of $GdLaO_3$ (ICSD#190648) with space group $C2/m$ (No. 12), and lattice parameters (a, b, c) = (14.433, 3.689, 8.997 Å) with a B-type monoclinic structure. Notably, when the Sc^{3+} concentration is below 10 mol%, no peaks related to the raw materials of Gd_2O_3, La_2O_3, Sc_2O_3, or any other impurities were detected, except for the signals originating from the $GdLaO_3$ host. However, when the Sc^{3+} concentration exceeds 10 mol%, Sc_2O_3 impurities are observed. The enlarged angular regions from 27° to 30° are shown in the right patterns of Fig. 1(a) and (b), respectively. Evidently, the

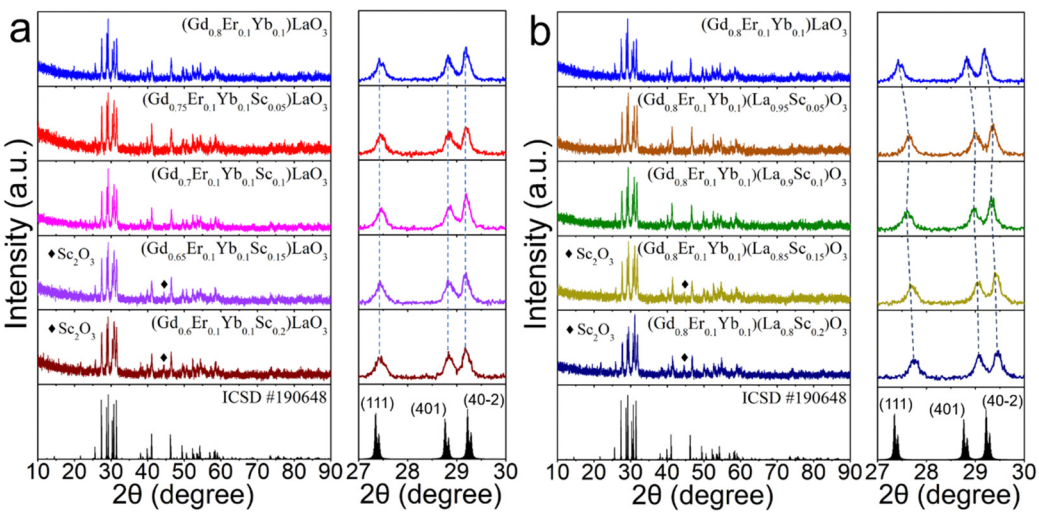

Fig. 1 Powder X-ray diffraction (XRD) patterns of $(Gd_{0.8-x}Er_{0.1}Yb_{0.1}Sc_x)LaO_3$ (x = 0, 0.05, 0.1, 0.15, 0.2) phosphors (a) and $(Gd_{0.8}Er_{0.1}Yb_{0.1})(La_{1-x}Sc_x)O_3$ (x = 0, 0.05, 0.1, 0.15, 0.2) phosphors (b). The standard pattern of $GdLaO_3$ (ICSD#190648) is presented as a reference. The right patterns in pictures (a) and (b) depict an enlarged angular region from 27° to 30°, respectively.

absence of peak shifting was confirmed when the sample was synthesized using stoichiometric means with Sc^{3+} ions molar replacing Gd^{3+} ions molar. However, when the sample was synthesized by stoichiometric means with Sc^{3+} ions molar replacing La^{3+} ions molar, the diffraction peaks shifted towards the smaller angle direction. This shows that the sintered sample with Sc^{3+} ions molar replacing La^{3+} ions molar has a more obvious structural change as the composition of Sc^{3+} increases than the sample with Sc^{3+} ions molar replacing Gd^{3+} ions molar, and the volume decreases as the doping of Sc^{3+} with a small radius increases.

The diffuse reflection (DR) spectra of $(Gd_{0.8}Er_{0.1}Yb_{0.1})LaO_3$, $(Gd_{0.8}Er_{0.1}Yb_{0.1}Sc_{0.1})LaO_3$, and $(Gd_{0.8}Er_{0.1}Yb_{0.1})(La_{0.9}Sc_{0.1})O_3$ phosphors are presented in Fig. 2(a). The absorption peaks in the DR spectra, ranging from 200 to 1800 nm, are mainly attributed to the transitions of Er^{3+} from $^4I_{15/2}$ to $^4G_{11/2}$, $^4F_{7/2}$, $^2H_{11/2}$, $^4F_{9/2}$, $^4I_{9/2}$, $^4I_{11/2}$, and $^4I_{13/2}$, respectively. Notably, these peaks at ~976 nm are from the transitions of Yb^{3+} from $^2F_{7/2}$ to $^2F_{5/2}$ and Er^{3+} from $^4I_{15/2}$ to $^4I_{11/2}$. Fig. 2(b) illustrates the corresponding bandgap values of the three phosphors, which are 4.61, 4.70, and 4.74 eV, respectively. Comparing the bandgap values among the three samples, this investigation reveals that the bandgap of the Er^{3+}/Yb^{3+} co-doped $GdLaO_3$ phosphor is smaller than that of the $Er^{3+}/Yb^{3+}/Sc^{3+}$ triple-doped $GdLaO_3$ phosphors. Furthermore, the bandgap value of the phosphor synthesized by stoichiometric means with Sc^{3+} ions molar replacing Gd^{3+} ions molar is smaller than that of the phosphor synthesized by stoichiometric means with Sc^{3+} ions molar replacing La^{3+} ions molar. Additionally, Fig. S1 (ESI†) displays the DR spectra and corresponding bandgap values for all samples. Fig. S2 (ESI†) presents relationships between bandgap and doped Sc^{3+} concentration in the $(Gd_{0.8-x}Er_{0.1}Yb_{0.1}Sc_x)LaO_3$ (x = 0, 0.05, 0.1, 0.15, 0.2) and $(Gd_{0.8}Er_{0.1}Yb_{0.1})(La_{1-x}Sc_x)O_3$ (x = 0, 0.05, 0.1, 0.15, 0.2) phosphors. The experimental results show that Sc^{3+} doping can increase the bandgap values. It is noteworthy that when the concentration of Sc^{3+} exceeds 10 mol%, the samples prepared by replacing La^{3+} ions molar with Sc^{3+} consistently exhibit a higher bandgap compared to the samples prepared by replacing Gd^{3+} ions molar with Sc^{3+}. The dosing according to different chemical formulas will lead to different lattice structures, which will change the bandgap values.

In order to confirm the positions occupied by $Er^{3+}/Yb^{3+}/Sc^{3+}$, we performed Rietveld refinement of the XRD data. For $(Gd_{0.8}Er_{0.1}Yb_{0.1})(La_{0.9}Sc_{0.1})O_3$, we first carried out the replacement of Rietveld refinement according to the molar ratio of raw materials, that is, supposing Er^{3+}/Yb^{3+} replaces Gd^{3+} and Sc^{3+} replaces La^{3+}. The result of this refinement is shown in Fig. S3(a) (ESI†). This refinement result is very unsatisfactory, and some peaks correspond very poorly, so it is unreasonable to refine according to the molar ratio of this chemical formula. Therefore, we assume that $Er^{3+}/Yb^{3+}/Sc^{3+}$ can randomly replace Gd^{3+} and La^{3+} sites for refinement. The refinement result is illustrated in Fig. 3(e). This refined result is more reasonable than Fig. S3(a) (ESI†). R_p is 12.6, and R_{wp} is 16, and these values are relatively high. Therefore, in order to verify the rationality of the above refinement, we conducted XRD slow scanning of the sample to improve the diffraction intensity of XRD, and then carried out the same refinement operation. R_p and R_{wp} become 4.32 and 5.55, respectively, as shown in Fig. S3(b) (ESI†). The R_p and R_{wp} values are very reasonable and once again confirm the accuracy of the structural refinement. With the same operation, the XRD results of $(Gd_{0.8}Er_{0.1}Yb_{0.1})LaO_3$ and $(Gd_{0.8}Er_{0.1}Yb_{0.1}Sc_{0.1})LaO_3$ are also refined, as shown in Fig. 3(a) and (c). For $(Gd_{0.8}Er_{0.1}Yb_{0.1})LaO_3$ and $(Gd_{0.8}Er_{0.1}Yb_{0.1}Sc_{0.1})LaO_3$,$Er^{3+}/Yb^{3+}$ replace the Gd^{3+}, Gd^{3+}/La^{3+}, and La^{3+} sites, and the distribution of Er^{3+}/Yb^{3+} in the host belongs to three-dimensional (3D). For $(Gd_{0.8}Er_{0.1}Yb_{0.1})(La_{0.9}Sc_{0.1})O_3$, Er^{3+}/Yb^{3+} replace the Gd^{3+} and Gd^{3+}/La^{3+} sites, and most Er^{3+}/Yb^{3+} replace the Gd^{3+} sites. Sc^{3+} replaces La^{3+} sites. Here, Er^{3+}/Yb^{3+} is distributed in a continuous double layer structure, blocked by a single layer of Sc^{3+}/La^{3+}. The distribution of Er^{3+}/Yb^{3+} in $(Gd_{0.8}Er_{0.1}Yb_{0.1})(La_{0.9}Sc_{0.1})O_3$ is the case between 3D and monolayer (2D). This structure can prevent the energy transfer between different bilayer structures and promote cross relaxation between Er^{3+} and Er^{3+}, Yb^{3+} and Er^{3+} in the double layers, and therefore is expected to obtain outstanding red UCL. In addition, the nearest distances between Yb^{3+} and Er^{3+} or Er^{3+} and Er^{3+} in the

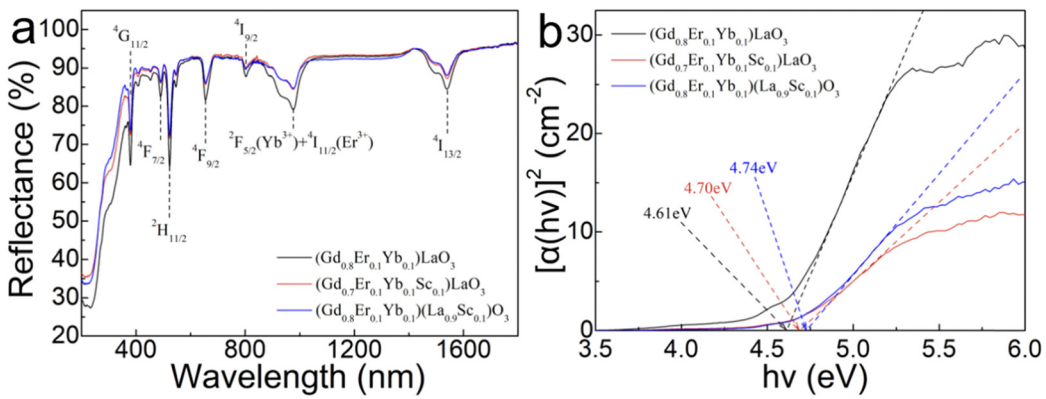

Fig. 2 (a) Diffuse reflectance spectra of $(Gd_{0.8}Er_{0.1}Yb_{0.1})LaO_3$, $(Gd_{0.8}Er_{0.1}Yb_{0.1}Sc_{0.1})LaO_3$, and $(Gd_{0.8}Er_{0.1}Yb_{0.1})(La_{0.9}Sc_{0.1})O_3$ phosphors. (b) Corresponding calculated bandgap values.

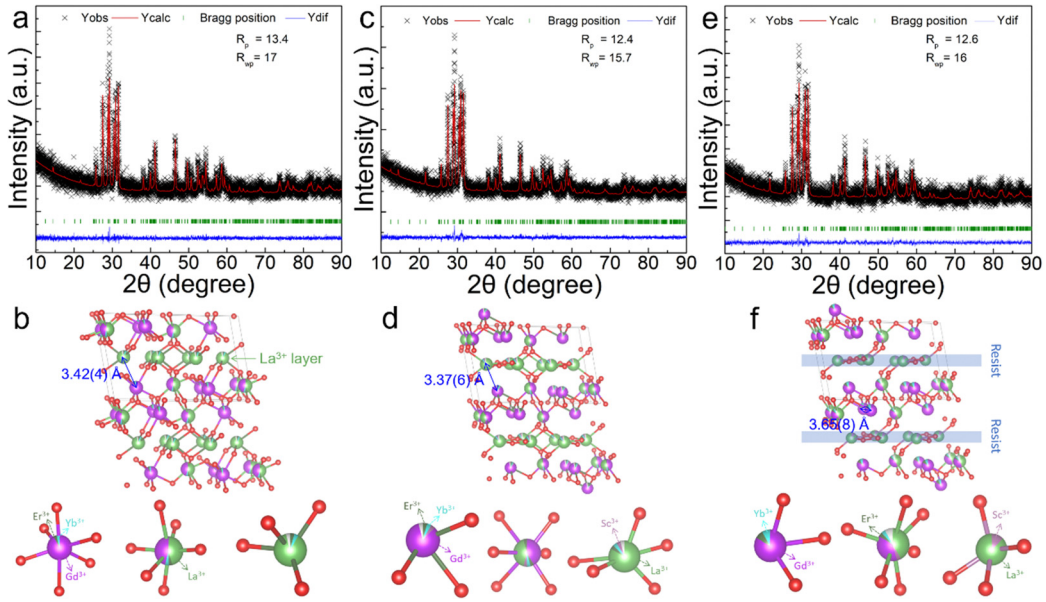

Fig. 3 Rietveld refinement of $(Gd_{0.8}Er_{0.1}Yb_{0.1})LaO_3$ (a), $(Gd_{0.8}Er_{0.1}Yb_{0.1}Sc_{0.1})LaO_3$ (c), and $(Gd_{0.8}Er_{0.1}Yb_{0.1})(La_{0.9}Sc_{0.1})O_3$ (e) phosphors. The crystal structures (b), (d), and (f) correspond to the above refined results, respectively. All the different coordination environments in $GdLaO_3$ are also shown below.

$(Gd_{0.8}Er_{0.1}Yb_{0.1})LaO_3$, $(Gd_{0.8}Er_{0.1}Yb_{0.1}Sc_{0.1})LaO_3$, and $(Gd_{0.8}Er_{0.1}Yb_{0.1})(La_{0.9}Sc_{0.1})O_3$ phosphors are 3.42(4), 3.37(6), and 3.65(8) Å, respectively, which are labeled in Fig. 3(b), (d), and (f).

Fig. 4(a) and (b) display the UCL spectra of $(Gd_{0.8-x}Er_{0.1}Yb_{0.1}Sc_x)LaO_3$ (x = 0, 0.1, 0.2) and $(Gd_{0.8}Er_{0.1}Yb_{0.1})(La_{1-x}Sc_x)O_3$ (x = 0, 0.1, 0.2) under 980 nm laser excitation. The samples with a concentration of 10 mol% Sc^{3+} exhibit the highest UCL intensity. The UCL spectra of other trivalent cation (Al^{3+}, Y^{3+}, Bi^{3+}, and La^{3+}) doped samples, respectively, replacing Gd^{3+} and La^{3+} in molar ratios for weighing, were also tested and shown in Fig. S4(a) and (c) (ESI†). The red UCL intensity integral areas are calculated and displayed in Fig. S4(b) and (d) (ESI†). This result shows that, compared with other trivalent elements, Sc^{3+} doping can obtain the highest red UCL intensity.

Fig. 5(a) depicts the red UCL integral intensity of the $(Gd_{0.8}Er_{0.1}Yb_{0.1})LaO_3$, $(Gd_{0.8}Er_{0.1}Yb_{0.1}Sc_{0.1})LaO_3$, $(Gd_{0.8}Er_{0.1}Yb_{0.1})(La_{0.9}Sc_{0.1})O_3$, and β-$NaYF_4$:$Er^{3+}$/$Yb^{3+}$ phosphor under 980 nm laser excitation with different excitation power densities. The red UCL intensity of all samples increases with increasing excitation power density. The UCL performance of $(Gd_{0.8}Er_{0.1}Yb_{0.1})(La_{0.9}Sc_{0.1})O_3$ is better than that of $(Gd_{0.8}Er_{0.1}Yb_{0.1}Sc_{0.1})LaO_3$, and much better than that of $(Gd_{0.8}Er_{0.1}Yb_{0.1})LaO_3$. Under 130.96 W cm^{-2}, the red UCL intensity of the $(Gd_{0.8}Er_{0.1}Yb_{0.1})(La_{0.9}Sc_{0.1})O_3$ sample reaches 100% of the strength exhibited by the commercial β-$NaYF_4$:Er^{3+}/Yb^{3+} phosphor. The corresponding UCL spectra are shown in Fig. 5(b) under 130.96 W cm^{-2} excitation.

The logarithmic curves of the red and green UCL intensity of $(Gd_{0.8}Er_{0.1}Yb_{0.1})LaO_3$, $(Gd_{0.8}Er_{0.1}Yb_{0.1}Sc_{0.1})LaO_3$, and $(Gd_{0.8}Er_{0.1}Yb_{0.1})(La_{0.9}Sc_{0.1})O_3$ as a function of the pump power density are shown in Fig. 6(a), (b) and (c), respectively. The relationship between the pump power density (P) and the integrated UCL intensity (I) in a multi-photon process can be expressed as follows:

$$\ln(I) \propto n \ln(P) \quad (1)$$

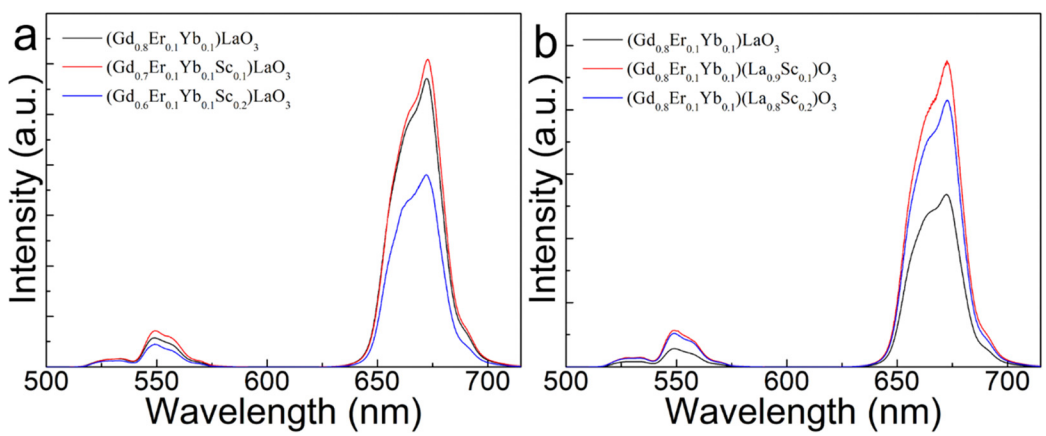

Fig. 4 UCL spectra of $(Gd_{0.8-x}Er_{0.1}Yb_{0.1}Sc_x)LaO_3$ (x = 0, 0.1, 0.2) (a) and $(Gd_{0.8}Er_{0.1}Yb_{0.1})(La_{1-x}Sc_x)O_3$ (x = 0, 0.1, 0.2) (b) under 980 nm laser excitation.

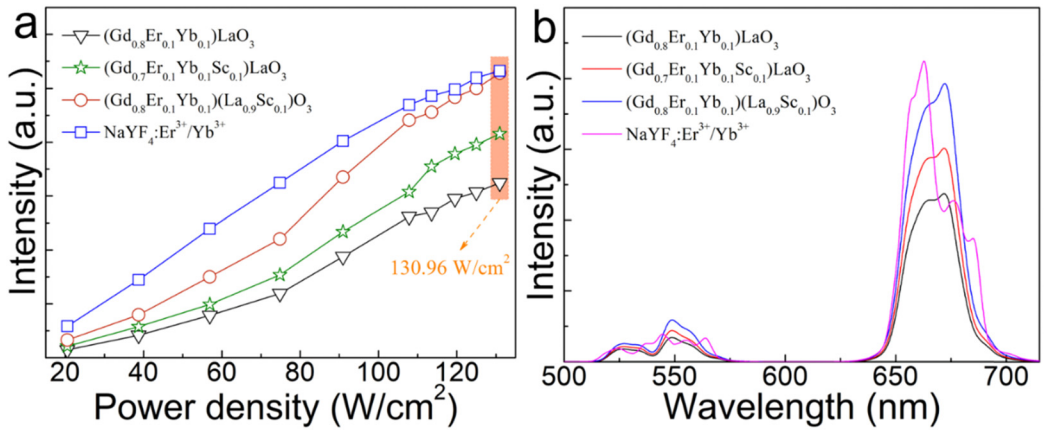

Fig. 5 (a) Red UCL integral intensity of $(Gd_{0.8}Er_{0.1}Yb_{0.1})LaO_3$, $(Gd_{0.8}Er_{0.1}Yb_{0.1}Sc_{0.1})LaO_3$, $(Gd_{0.8}Er_{0.1}Yb_{0.1})(La_{0.9}Sc_{0.1})O_3$, and commercial β-$NaYF_4:Er^{3+}$/$Yb^{3+}$ phosphors under 980 nm laser excitation with different excitation power densities. (b) UCL spectra when the pump power density of the 980 nm laser was fixed at 130.96 W cm^{-2}.

where n is the number of photons. The linear fitting of the integrated red UCL yields slope n values of 1.997, 1.855, and 2.134 for $(Gd_{0.8}Er_{0.1}Yb_{0.1})LaO_3$, $(Gd_{0.8}Er_{0.1}Yb_{0.1}Sc_{0.1})LaO_3$, and $(Gd_{0.8}Er_{0.1}Yb_{0.1})(La_{0.9}Sc_{0.1})O_3$, respectively. Similarly, the corresponding green UCL slope n values are 2.199, 2.070, and 2.320, respectively. Fig. 6(d) illustrates the relationship between n values and the nearest distance between Yb^{3+} and Er^{3+} or Er^{3+} and Er^{3+}. This result shows that the change in n value is related to the nearest distance, and for the $GdLaO_3$ host, the n value increases with the increase in the nearest distance. This indicates that the n value is closely related to the energy transfer efficiency from CR between Yb^{3+} and Er^{3+} or Er^{3+} and Er^{3+} under 980 nm laser excitation.

The possible UCL luminescence process under 980 nm pump excitation is illustrated in Fig. 7. UCL processes contain ground state absorption (GSA), excited state absorption (ESA),

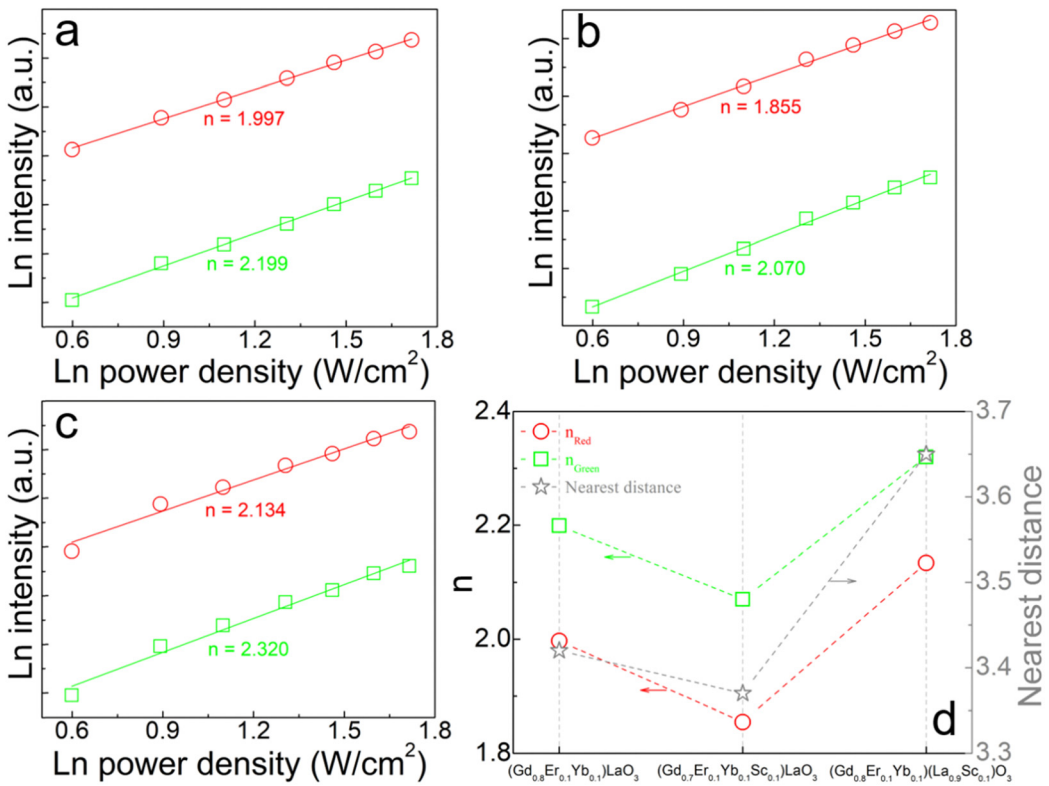

Fig. 6 Double logarithmic plots of the integrated red and green UCL intensity as a function of pump power of (a) $(Gd_{0.8}Er_{0.1}Yb_{0.1})LaO_3$, (b) $(Gd_{0.8}Er_{0.1}Yb_{0.1}Sc_{0.1})LaO_3$, and (c) $(Gd_{0.8}Er_{0.1}Yb_{0.1})(La_{0.9}Sc_{0.1})O_3$. (d) Relationship between the slope of the curve and nearest distance between Yb^{3+} and Er^{3+} or Er^{3+} and Er^{3+} in the host.

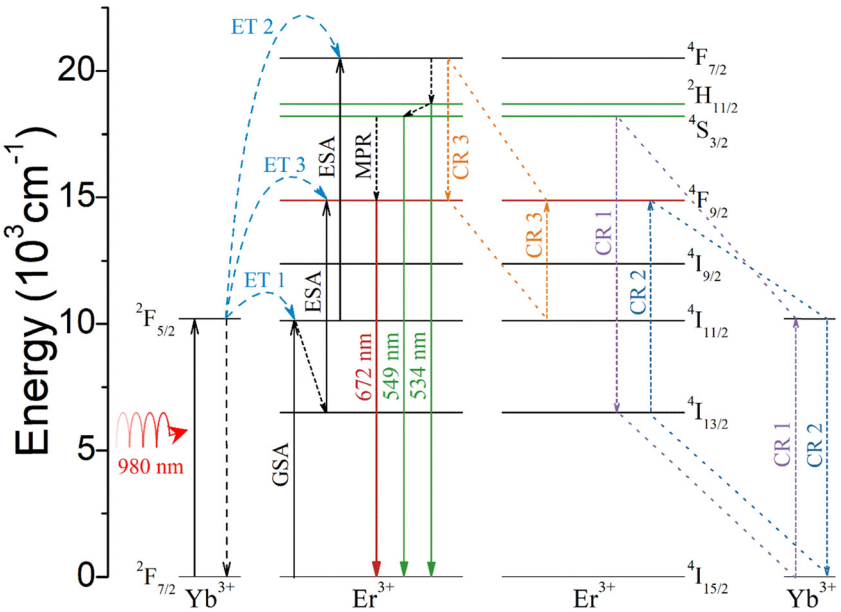

Fig. 7 Schematic illustration of possible UC emission processes under 980 nm laser excitation.

energy transfer (ET), multiphonon non-radiative transition (MPR), and cross relaxation (CR). The CR process is significantly related to the distance between Yb^{3+} and Er^{3+} or Er^{3+} and Er^{3+}. Yb^{3+} exhibits a large absorption cross section of 980 nm, and the electron absorbs 980 nm light energy and jumps from $^2F_{7/2}$ to $^2F_{5/2}$. Firstly, Er^{3+} undergoes two energy transfers from Yb^{3+}: $^4I_{15/2}$ (Er^{3+}) + $^2F_{5/2}$ (Yb^{3+}) → $^4I_{11/2}$ (Er^{3+}) + $^2F_{7/2}$ (Yb^{3+}) (ET 1) and $^4I_{11/2}$ (Er^{3+}) + $^2F_{5/2}$ (Yb^{3+}) → $^4F_{7/2}$ (Er^{3+}) + $^2F_{7/2}$ (Yb^{3+}) (ET 2), resulting in the population of $^4F_{7/2}$ of Er^{3+}. The $^2H_{11/2}$ and $^4S_{3/2}$ are then populated through MPR, resulting in green light emission through radiative transitions with $^2H_{11/2}$ → $^4I_{15/2}$ and $^4S_{3/2}$ → $^4I_{15/2}$ in Er^{3+}. $^4F_{9/2}$ in Er^{3+} can be populated through MPR with $^4S_{3/2}$ → $^4F_{9/2}$. However, due to the low phonon energy of the $GdLaO_3$ host, MPR with $^4S_{3/2}$ → $^4F_{9/2}$ is weak. Therefore, it is believed that this transition pathway is not the main reason for the strong red UCL emission. Additionally, the red UCL pathway also involves electrons that are populated at $^4I_{13/2}$ through MPR with $^4I_{11/2}$ → $^4I_{13/2}$ and then jump to $^4F_{9/2}$ through energy transfer: $^4I_{13/2}$ (Er^{3+}) + $^2F_{5/2}$ (Yb^{3+}) → $^4F_{9/2}$ (Er^{3+}) + $^2F_{7/2}$ (Yb^{3+}) (ET 3), resulting in red UCL emission. However, this MPR with $^4I_{11/2}$ → $^4I_{13/2}$ is also weak, so this transition pathway should not be the main cause of the intense red UCL emission. In addition, red UCL emission can be achieved by CR 1, CR 2, and CR 3. In general, for oxide UCL phosphors with low phonon energy, red UCL should come mainly from CR, which has also been discussed in detail in some other studies.[35–38] The three CR 1, CR 2 and CR 3 processes involve the following transitions: $^4S_{3/2}$ (Er^{3+}) + $^2F_{7/2}$ (Yb^{3+}) → $^4I_{13/2}$ (Er^{3+}) + $^2F_{5/2}$ (Yb^{3+}) (CR 1), $^4I_{13/2}$ (Er^{3+}) + $^2F_{5/2}$ (Yb^{3+}) → $^4F_{9/2}$ (Er^{3+}) + $^2F_{7/2}$ (Yb^{3+}) (CR 2), and $^4F_{7/2}$ (Er^{3+}) + $^4I_{11/2}$ (Er^{3+}) → $^4F_{9/2}$ (Er^{3+}) + $^4F_{9/2}$ (Er^{3+}) (CR 3). CR 1 can reduce the populated electron number at $^4S_{3/2}$, which produces green UCL. CR 2 and CR 3 can enhance the electron population of $^4F_{9/2}$ in Er^{3+} with emitting red UCL. In summary, the strong red UCL emission mainly comes from the simultaneous occurrence of CR 1 and CR 2 between Er^{3+} and Yb^{3+}, and CR 3 between Er^{3+} and Er^{3+}. For $(Gd_{0.8}Er_{0.1}Yb_{0.1})(La_{0.9}Sc_{0.1})O_3$, Er^{3+} and Yb^{3+} are distributed in a continuous double layer structure, blocked by a single layer of Sc^{3+}/La^{3+}. Therefore, this structure allows CR 1, CR 2, and CR 3 to occur only in the double-layer structure and improves the efficiency of energy transfer with CR 1, CR 2, and CR 3 in the double-layer. These CR 1 and CR 2 will make the number of photons n emitted by red light become super-quadratic dependence of the red intensity on 980 nm laser power density. CR 3 will cause a sub-quadratic dependence of red intensity on 980 nm laser power density because three 980 nm photons generate two red photons.[38] Therefore, for $(Gd_{0.8}Er_{0.1}Yb_{0.1})LaO_3$ and $(Gd_{0.8}Er_{0.1}Yb_{0.1}Sc_{0.1})LaO_3$, CR 3 may have a major role. For $(Gd_{0.8}Er_{0.1}Yb_{0.1})(La_{0.9}Sc_{0.1})O_3$, CR 1 and CR 2 may play a major role. In these three samples, the difference in photon number n and the difference in electron transition path should be due to the difference in $Er^{3+}/Yb^{3+}/Sc^{3+}$ substitution positions and the change in distance between Er^{3+} and Yb^{3+} or Er^{3+} and Er^{3+}.

Fig. 8(a) illustrates the temperature-dependent UCL spectra of $(Gd_{0.8}Er_{0.1}Yb_{0.1})(La_{0.9}Sc_{0.1})O_3$ within the temperature range of 303–663 K under 980 nm laser excitation. It has been demonstrated that the UCL integral intensity decreases as the temperature increases. To evaluate the temperature sensing property of $(Gd_{0.8}Er_{0.1}Yb_{0.1})(La_{0.9}Sc_{0.1})O_3$, the UCL integral intensity of $^2H_{11/2}$ → $^4I_{15/2}$ (I_H), $^4S_{3/2}$ → $^4I_{15/2}$ (I_S), and $^4F_{9/2}$ → $^4I_{15/2}$ (I_F) were calculated under different temperatures. The LIR (I_H/I_S, I_H/I_F) values and their relationship with temperature can be calculated and fitted using the following formula:

$$LIR_1 = \frac{I_H}{I_S} = B_1 \exp^{\frac{-\Delta E_1}{K_B T}} \quad (2)$$

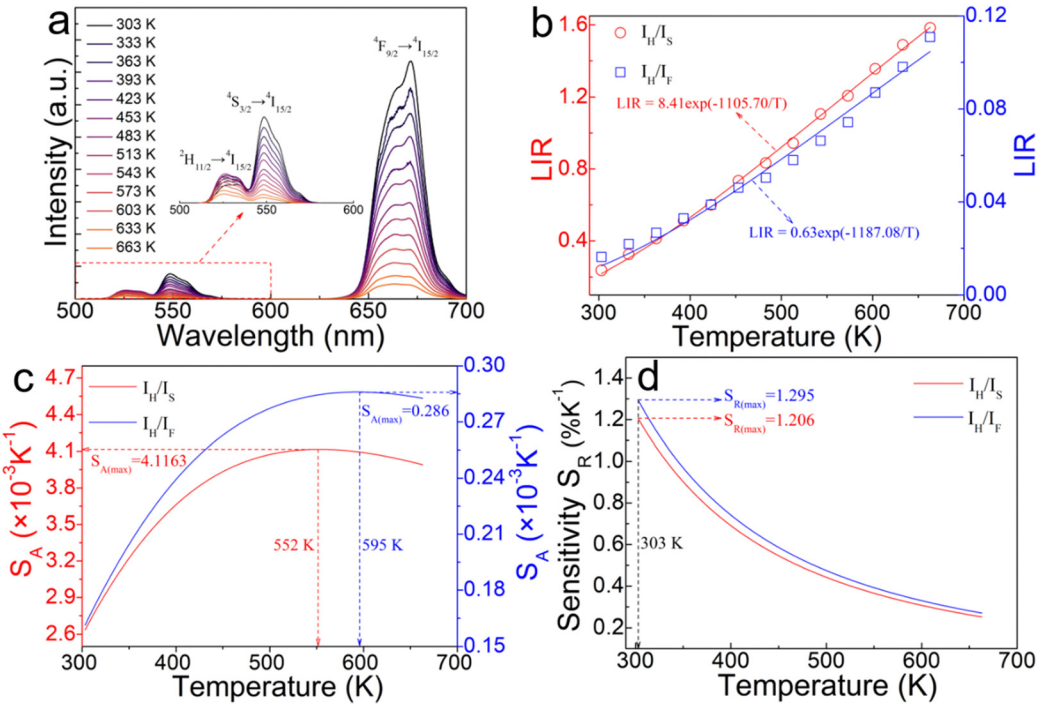

Fig. 8 (a) Temperature-dependent UCL emission spectra of the $(Gd_{0.8}Er_{0.1}Yb_{0.1})(La_{0.9}Sc_{0.1})O_3$ phosphor at 303–663 K under 980 nm laser excitation. The inset shows an enlarged wavelength region from 500 to 600 nm. (b) Relationship between LIR values and temperature. (c) Absolute sensitivity (S_A). (d) Relative sensitivity (S_R).

$$\mathrm{LIR}_2 = \frac{I_H}{I_F} = B_2 \exp^{\frac{-\Delta E_2}{K_B T}} \quad (3)$$

B_1 and B_2 are constants, and ΔE_1 and ΔE_2 represent the bandgaps between the energies $^2H_{11/2}$ and $^4S_{3/2}$, $^2H_{11/2}$ and $^4F_{9/2}$, respectively, K_B is the Boltzmann constant, and T is the absolute temperature. The experimental results are depicted in Fig. 8(b). Based on the data presented in Fig. 8(b), the absolute sensitivity (S_A) and relative sensitivity (S_R) can be calculated as follows:

$$S_A = \frac{\mathrm{dLIR}}{\mathrm{d}T} = B\frac{\Delta E}{K_B T^2}\exp^{\frac{-\Delta E}{K_B T}} \quad (4)$$

$$S_R = \frac{1}{\mathrm{LIR}}\frac{\mathrm{dLIR}}{\mathrm{d}T} = \frac{\Delta E}{K_B T^2} \quad (5)$$

The experimental results of absolute sensitivity (S_A) and relative sensitivity (S_R) are presented in Fig. 8(c) and (d), respectively. The maximum values of absolute sensitivity (S_A) are 0.004116 K^{-1} at 552 K and 0.000286 K^{-1} at 595 K, respectively. Similarly, the maximum values of the relative sensitivities (S_R) are 0.01206 K^{-1} and 0.01295 K^{-1} at 303 K, respectively. The maximum absolute and relative sensitivity are compared with other materials, as shown in Table 1. This result indicates that $(Gd_{0.8}Er_{0.1}Yb_{0.1})(La_{0.9}Sc_{0.1})O_3$ exhibits excellent temperature sensing performance under 980 nm laser excitation and holds promising potential for temperature sensing applications.

Table 1 Values of maximum absolute sensitivity (S_A) and relative sensitivity (S_R) of different materials

Materials	S_A (K^{-1})	S_R (K^{-1})	Ref.
$SrLu_2O_4:Er^{3+}/Yb^{3+}$	0.00126	0.00260	39
$BiLaWO_6:Er^{3+}/Tm^{3+}/Yb^{3+}$	0.00120	0.00430	40
$Ba_3Y_4O_9:Er^{3+}/Yb^{3+}$	0.00371	—	41
$Gd_2(WO_4)_3:Er^{3+}/Yb^{3+}$	0.00130	—	42
$NaGdF_4:Er^{3+}$	0.001	—	43
$Gd_2O_3:Er^{3+}@Gd_2O_3:Yb^{3+}$	0.0007	—	44
$LaGdO_3:Er^{3+}/Yb^{3+}$	0.0034	0.0108	45
$BaY_2O_4:Er^{3+}/Yb^{3+}$	0.0019	—	46
$(Gd_{0.8}Er_{0.1}Yb_{0.1})(La_{0.9}Sc_{0.1})O_3$	0.0041163	0.01295	This work

4. Conclusion

$GdLaO_3:Er^{3+}/Yb^{3+}/Sc^{3+}$ phosphors with space group $C2/m$ (No. 12) are successfully synthesized by high temperature solid state sintering and have excellent red UCL intensity. $(Gd_{0.8}Er_{0.1}Yb_{0.1})(La_{0.9}Sc_{0.1})O_3$ represents the highest red UCL intensity in all the samples, which is comparable to commercial red β-$NaYF_4:Er^{3+}/Yb^{3+}$. The Rietveld refinement result of the XRD data reveals that Er^{3+}/Yb^{3+} are distributed in a continuous double layer structure, blocked by a single layer of Sc^{3+}/La^{3+}. This special structure allows cross relaxation between Er^{3+} and Er^{3+}, Er^{3+} and Yb^{3+} to occur only in the double-layer structure and improves the efficiency of energy transfer with cross relaxation in the double-layer. The maximum value of relative temperature sensitivity reaches 0.01295 K^{-1} at 303 K. $GdLaO_3:Er^{3+}/Yb^{3+}/Sc^{3+}$ phosphors with excellent pure red UCL

emission have good application prospects in luminescence display and temperature sensing.

Conflicts of interest

There are no conflicts of interest to declare.

Acknowledgements

This study was supported in part by NSFC (National Natural Science Foundation of China, grant no. 11774042, 52071048 and 51772159), Fundamental Research Funds for the Central Universities (grant no. 3132023196 and 3132023519), and China Postdoctoral Science Foundation (grant no. 2016M591420 and 3620080711).

References

1 F. Auzel, History of upconversion discovery and its evolution, *J. Lumin.*, 2020, **223**, 116900.
2 K. Li and R. Van Deun, $Ca_3La_2Te_2O_{12}$:Mn^{4+}, Nd^{3+}, Yb^{3+}: an efficient thermally-stable UV/visible-far red/NIR broadband spectral converter for c-Si solar cells and plant-growth LEDs, *Mater. Chem. Front.*, 2019, **3**, 403–413.
3 H. Rodríguez-Rodríguez, M. H. Imanieh, F. Lahoz and I. R. Martín, Analysis of the upconversion process in Tm^{3+} doped glasses for enhancement of the photocurrent in silicon solar cells, *Sol. Energy Mater. Sol. Cells*, 2016, **144**, 29–32.
4 X. Zhao, F. Liu, T. Shi, H. Wu, L. Zhang, J. Zhang, X. Wang and Y. Liu, Conceptual ultraviolet-C light source based on up-conversion luminescence, *Adv. Photonics Res.*, 2022, **3**, 2200106.
5 L. Lei, D. Chen, C. Li, F. Huang, J. Zhang and S. Xu, Inverse thermal quenching effect in lanthanide-doped upconversion nanocrystals for anti-counterfeiting, *J. Mater. Chem. C*, 2018, **6**, 5427.
6 J. Ruan, Z. Yang, Y. Wen, M. Li, Y. Ren, J. Qiu, Z. Song and Y. Wang, Laser induced thermochromism and reversible upconversion emission modulation of a novel WO_3:Yb^{3+}, Er^{3+} ceramic: dual-modal fingerprint acquisition application, *Chem. Eng. J.*, 2020, **383**, 123180.
7 B. Chen and F. Wang, Recent advances in the synthesis and application of Yb-based fluoride upconversion nanoparticles, *Inorg. Chem. Front.*, 2020, **7**, 1067.
8 M. Bettinelli, L. Carlos and X. Liu, Lanthanide-doped upconversion nanoparticles, *Phys. Today*, 2015, **68**, 38–44.
9 C. D. S. Brites, R. Marin, M. Suta, A. N. Carneiro Neto, E. Ximendes, D. Jaque and L. D. Carlos, Spotlight on luminescence thermometry: basics, challenges, and cutting-edge applications, *Adv. Mater.*, 2023, **35**, 2302749.
10 K. Maciejewska, A. Bednarkiewicz, A. Meijerink and L. Marciniak, Correlation between the covalency and the thermometric properties of Yb^{3+}/Er^{3+} codoped nanocrystalline orthophosphates, *J. Phys. Chem. C*, 2021, **125**, 2659–2665.
11 K. Zheng, W. Song, G. He, Z. Yuan and W. Qin, Five-photon UV upconversion emissions of Er^{3+} for temperature sensing, *Opt. Express*, 2015, **23**, 7653–7658.
12 R. Shi, C. D. S. Brites and L. D. Carlos, Hexagonal-phase $NaREF_4$ upconversion nanocrystals: the matter of crystal structure, *Nanoscale*, 2021, **13**, 19771–19782.
13 C. Renero-Lecuna, R. Martín-Rodríguez, R. Valiente, J. González, F. Rodríguez, K. W. Krämer and H. U. Güdel, Origin of the high upconversion green luminescence efficiency in β-$NaYF_4$:2%Er^{3+}, 20%Yb^{3+}, *Chem. Mater.*, 2011, **23**, 3442–3448.
14 H. Dong, L. D. Sun and C. H. Yan, Basic understanding of the lanthanide related upconversion emissions, *Nanoscale*, 2013, **5**, 5703–5714.
15 H. Wu, Z. Hao, L. Zhang, X. Zhang, Y. Xiao, G. H. Pan, H. Wu, Y. Luo, H. Zhao and J. Zhang, Phonon energy dependent energy transfer upconversion for the red emission in the Er^{3+}/Yb^{3+} system, *J. Phys. Chem. C*, 2018, **122**, 9611–9618.
16 W. You, D. Tu, W. Zheng, P. Huang and X. Chen, Lanthanide-doped disordered crystals: Site symmetry and optical properties, *J. Lumin.*, 2018, **201**, 255–264.
17 H. Suo, X. Zhao, Z. Zhang, R. Shi, Y. Wu, J. Xiang and C. Guo, Local symmetric distortion boosted photon upconversion and thermometric sensitivity in lanthanum oxide nanospheres, *Nanoscale*, 2018, **10**, 9245–9251.
18 H. Dong, L. D. Sun and C. H. Yan, Local structure engineering in lanthanide-doped nanocrystals for tunable upconversion emissions, *J. Am. Chem. Soc.*, 2021, **143**, 20546–20561.
19 F. T. Rabouw, P. T. Prins, P. Villanueva-Delgado, M. Castelijns, R. G. Geitenbeek and A. Meijerink, Quenching pathways in $NaYF_4$:Er^{3+}, Yb^{3+} upconversion nanocrystals, *ACS Nano*, 2018, **12**, 10576–10577.
20 H. Bae, D. Park, K. Shin, H. Lee, K. M. Ok and K. T. Lee, Upconversion properties in lanthanide doped layered-perovskite, $CsBiNb_2O_7$, *J. Chem. Phys.*, 2021, **154**, 054701.
21 N. Zhang, M. S. Molokeev, Q. Liu and Z. Xia, Pure red upconversion luminescence and optical thermometry of Er^{3+} doped sensitizer-rich $SrYbInO_4$ phosphors, *J. Mater. Chem. C*, 2018, **6**, 7361–7366.
22 L. Feng, Z. Hao, Y. Luo, X. Zhang, L. Zhang, G. Pan, H. Wu and J. Zhang, Observation and photoluminescence properties of two Er^{3+} centers in $CaSc_2O_4$:Er^{3+}, Yb^{3+} upconverting phosphor, *J. Alloys Compd.*, 2017, **708**, 827–833.
23 H. Cui, Y. Cao, Y. Zhang, L. Cao, S. Ran, X. Wang, D. Wu, X. Li, X. Zhang and B. Chen, Extremely intense green upconversion luminescent and ultra-high temperature sensitivity in Er^{3+}/Yb^{3+}co-doped $BiTa_7O_{19}$ phosphors, *J. Lumin.*, 2022, **241**, 118484.
24 L. Li, Y. Cao, Y. Zhang, H. Cui, G. Li, J. Zhang, X. Zhang and B. Chen, Excellent upconversion luminescence intensity in Er^{3+}/Yb^{3+}/Mo^{4+} triple-doped $BiTa_7O_{19}$ phosphors, *J. Alloys Compd.*, 2023, **938**, 168725.
25 X. Yan, Y. Cao, T. Liu, X. Wang, L. Li, J. Zhang and B. Chen, Order-disorder phase transitions significantly improving the upconversion luminescence intensity of $BiTa_7O_{19}$:Er^{3+}/Yb^{3+}, *Ceram. Int.*, 2024, **50**, 9433–9440.

26 S. P. Pavunny, A. Kumar, P. Misra, J. F. Scott and R. S. Katiyar, Properties of the new electronic device material $LaGdO_3$, *Phys. Status Solidi B*, 2014, **251**, 131–139.
27 G. A. Tompsett, R. J. Phillips, N. M. Sammes and A. M. Cartner, Characterisation of $LaGdO_3$ by X-ray powder diffraction and Raman spectroscopy, *Solid State Commun.*, 1998, **108**, 655–660.
28 G. T. Xiang, M. Xiong, Z. Y. Yang, Y. J. Wang, L. Yao, S. Jiang, X. J. Zhou, L. Li, X. J. Wang and J. H. Zhang, Multipath optical thermometry realized by electronic levels and stark sublevels of Er^{3+}, *Ceram. Int.*, 2024, **50**, 5261–5266.
29 G. T. Xiang, Y. Y. Yi, Z. Y. Yang, Y. J. Wang, L. Yao, S. Jiang, X. J. Zhou, L. Li, X. J. Wang and J. H. Zhang, Achieving ultrasensitive temperature sensing through non-thermally coupled energy levels to overcome energy gap constraints, *Inorg. Chem. Front.*, 2024, **11**, 1522–1530.
30 P. Li, L. Guo, C. Liang, T. Li and P. Chen, Enhanced dual-wavelength sensitive upconversion luminescence of $BiPO_4$:Yb^{3+}/Er^{3+} phosphors by Sc^{3+} doping, *Mater. Sci. Eng. B*, 2018, **229**, 20–26.
31 C. Zhang, Q. Jiang, M. Liu, H. Ma and Y. Kuai, Enhanced upconversion luminescent properties of KYb_2F_7:Er^{3+} by Sc^{3+} doping, *Opt. Mater.*, 2019, **88**, 615–620.
32 Y. Wang, C. Zuo, C. Ma, W. Ye, C. Zhao, Z. Feng, Y. Li, Z. Wen, C. Wang, X. Shen, X. Yuan and Y. Cao, Effects of Sc^{3+} ions on local crystal structure and up-conversion luminescence of layered perovskite $NaYTiO_4$:Yb^{3+}/Er^{3+}, *J. Alloys Compd.*, 2021, **876**, 160166.
33 M. M. Liu, G. C. Zheng, Y. Wei, D. Tian, Q. B. Zheng, L. Huang and J. Xie, Doping induced morphology, crystal structure, and upconversion luminescence evolution: from Na_3ScF_6:Yb/Er/Y to $NaYF_4$:Yb/Er/Sc nanocrystals, *Rare Met.*, 2023, **42**, 1018–1027.
34 B. H. Toby, EXPGUI, a graphical user interface for GSAS, *J. Appl. Cryst.*, 2001, **34**, 210–213.
35 G. Xiang, Q. Xia, S. Xu, X. Liu, S. Jiang, Y. Wang, X. Zhou, L. Li, L. Ma, X. Wang and J. Zhang, Multipath optical thermometry realized in $CaSc_2O_4$:Yb^{3+}/Er^{3+} with high sensitivity and superior resolution, *J. Am. Ceram. Soc.*, 2021, **104**, 2711–2720.
36 J. Zhang, Z. Hao, J. Li, X. Zhang, Y. Luo and G. Pan, Observation of efficient population of the red-emitting state from the green state by non-multiphonon relaxation in the Er^{3+}-Yb^{3+} system, *Light: Sci. Appl.*, 2015, **4**, e239.
37 C. Mi, J. Wu, Y. Yang, B. Han and J. Wei, Efficient upconversion luminescence from $Ba_5Gd_8Zn_4O_{21}$:Yb^{3+}, Er^{3+} based on a demonstrated cross-relaxation process, *Sci. Rep.*, 2016, **6**, 22545.
38 J. L. Sommerdijk and A. Bril, Visible luminescence of Yb^{3+}, Er^{3+} under IR excitation, Luminescence of Crystals, Molecules, and Solutions: Proceedings of the International Conference on Luminescence held in Leningrad, USSR, August 1972. Boston, MA: Springer US, 1972, pp. 86–91.
39 Y. Jina, X. Luoa, Z. Zhoua, R. Rana, S. Tana, H. Linb, F. Mengb, G. Xiangc, L. Mad and X. Wang, The excellent dual optical thermometry of the Yb^{3+}, Er^{3+} doped $SrLu_2O_4$, *J. Lumin.*, 2022, **251**, 119260.
40 K. Pavani, A. J. Neves, R. J. B. Pinto, C. S. R. Freire, M. J. Soares, M. P. F. Graça, K. U. Kumar and S. K. Jakka, $BiLaWO_6$:Er^{3+}/Tm^{3+}/Yb^{3+}phosphor: Study of multiple fluorescence intensity ratiometric thermometry at cryogenic temperatures, *Ceram. Int.*, 2022, **48**, 31344–31353.
41 H. Wu, Z. Hao, L. Zhang, X. Zhang, Y. Xiao, G. H. Pan, H. Wu, Y. Luo, L. Zhang and J. Zhang, Er^{3+}/Yb^{3+} codoped phosphor $Ba_3Y_4O_9$ with intense red upconversion emission and optical temperature sensing behavior, *J. Mater. Chem. C*, 2018, **6**, 3459–3467.
42 H. Lu, R. Meng, H. Hao, Y. Bai, Y. Gao, Y. Song, Y. Wang and X. Zhang, Stark sublevels of Er^{3+}-Yb^{3+} codoped $Gd_2(WO_4)_3$ phosphor for enhancing the sensitivity of a luminescent thermometer, *RSC Adv.*, 2016, **6**, 57667–57671.
43 Y. Bu, L. Meng and X. Yan, Tm^{3+} modified optical temperature behavior of transparent Er^{3+}-doped hexagonal $NaGdF_4$ glass ceramics, *Nanoscale Res. Lett.*, 2017, **12**, 402.
44 Z. Liu, R. X. Wang, K. W. Sun, X. C. Ling, J. W. Sun and D. H. Chen, Upconversion red light emission and luminescence thermometry of Gd_2O_3:Er^{3+}@Gd_2O_3:Yb^{3+} core-shell nanofibers synthesized via electrospinning, *Chalcogenide Lett.*, 2023, **20**, 439–447.
45 A. Siaï, P. Haro-González, K. H. Naifer and M. Férid, Optical temperature sensing of Er^{3+}/Yb^{3+} doped $LaGdO_3$ based on fluorescence intensity ratio and lifetime thermometry, *Opt. Mater.*, 2018, **76**, 34–41.
46 G. Xiang, X. Liu, Q. Xia, S. Jiang, X. Zhou, L. Li, Y. Jin, L. Ma, X. Wang and J. Zhang, Deep-tissue temperature sensing realized in BaY_2O_4:Yb^{3+}/Er^{3+} with ultrahigh sensitivity and extremely intense red upconversion luminescence, *Inorg. Chem.*, 2020, **59**, 11054–11060.